JGR Oceans

RESEARCH ARTICLE
10.1029/2024JC021463

The Bering Strait Throughflow Component of the Global Mass, Heat and Freshwater Transport

Xiaoting Yang[1] and **Paola Cessi**[1]

[1]Scripps Institution of Oceanography, University of California, San Diego, CA, USA

Key Points:

- Bering Strait throughflow is part of the mid-depth overturning with the upper branch in the Pacific and the lower branch in the Atlantic
- Bering Strait throughflow carries heat northward everywhere
- Bering Strait throughflow carries freshwater northward in the Pacific but southward in the Atlantic, enhancing the salt-advection feedback

Supporting Information:

Supporting Information may be found in the online version of this article.

Correspondence to:

P. Cessi,
pcessi@ucsd.edu

Citation:

Yang, X., & Cessi, P. (2024). The Bering Strait throughflow component of the global mass, heat and freshwater transport. *Journal of Geophysical Research: Oceans*, *129*, e2024JC021463. https://doi.org/10.1029/2024JC021463

Received 13 JUN 2024
Accepted 24 SEP 2024

Author Contributions:

Conceptualization: Xiaoting Yang, Paola Cessi
Formal analysis: Xiaoting Yang, Paola Cessi
Funding acquisition: Paola Cessi
Methodology: Xiaoting Yang, Paola Cessi
Software: Xiaoting Yang, Paola Cessi
Supervision: Paola Cessi
Visualization: Xiaoting Yang, Paola Cessi
Writing – original draft: Xiaoting Yang, Paola Cessi

Abstract As the only oceanic connection between the Pacific and Arctic-Atlantic Oceans, Bering Strait throughflow carries a climatological northward transport of about 1 Sv, contributing to the Atlantic Meridional Overturning Circulation (AMOC). Here, Lagrangian analysis quantifies the global distributions of volume transport, transit-times, thermohaline properties, diapycnal transformation, heat and freshwater transports associated with Bering Strait throughflow. Virtual Lagrangian parcels, released at Bering Strait, are advected by the velocity of Estimating the Circulation and Climate of the Ocean, backward and forward in time. Backward trajectories reveal that Bering Strait throughflow enters the Pacific basin on the southeast side, as part of fresh Antarctic Intermediate Water, then follows the wind-driven circulation to Bering Strait. Median transit time from 30°S in Indo-Pacific to Bering Strait is 175 years. Sixty-four percent of Bering Strait throughflow enters the North Atlantic through the Labrador Sea. The remaining 36% flows through the Greenland Sea, warmed and salinified by the northward flowing Atlantic waters. Deep water formation of water flowing through Bering Strait occurs predominantly in the Labrador Sea. Subsequently, this water joins the lower branch of AMOC, flowing southward in the deep western boundary current as North Atlantic Deep Water. Median transit time from Bering Strait to 30°S in South Atlantic is 160 years. The net heat transport of Bering Strait throughflow is northward everywhere, and net freshwater transport by Bering Strait throughflow is mostly northward. The freshwater transport is largest in the subpolar region of basin sectors: northward in the Pacific and Arctic and southward in the Atlantic.

Plain Language Summary The only oceanic connection between the North Pacific and the Arctic and North Atlantic is through Bering Strait. This small passage allows transport of mass, heat and salt. The contribution of the Bering Strait throughflow to the global overturning circulation is isolated using computer-generated floats that follow for 1,500 years the waters passing through Bering Strait in their global journey. These virtual-float trajectories start in the southeast Pacific above 1,000 m and flow northward, getting shallower, fresher and colder. After entering the Arctic through Bering Strait, parcels access the North Atlantic primarily from the Labrador Sea (64%) and Greenland Sea (36%). In these regions they get denser and enter the lower, southward branch of the Atlantic Meridional Overturning Circulation, taking about 350 years to reach the South Atlantic at 30° S from the same latitude in the South Pacific. The Bering Strait throughflow contributes to the global mid-depth overturning with its upper, northward branch in the Pacific and the lower, southward branch in the Atlantic. This cell carries heat everywhere northward because it flows northward at higher temperatures and fresher waters in the Pacific than the southward flow in the Atlantic.

1. Introduction

The mid-depth meridional overturning circulation (MOC) is primarily confined to the Atlantic basin (Atlantic Meridional Overturning Circulation, AMOC). In the Atlantic, the AMOC carries heat northward at every latitude, including the southern hemisphere, and freshwater southward, although the Atlantic is a net-evaporative basin (Ferreira et al., 2018). The southward freshwater transport supports a salt-advection feedback which makes the AMOC potentially unstable to high-latitudes freshwater perturbations (Cimatoribus et al., 2012; Rahmstorf, 1996; Stommel, 1961). The general consensus is that the AMOC is responsible for southward freshwater transport in the Atlantic, while the transport associated with net volume transport plus the gyral circulation (i.e., the "azonal" circulation), transport freshwater northward (Drijfhout et al., 2011; L. C. Jackson & Wood, 2018; Mecking et al., 2016). The attribution of the freshwater (or heat) transports to different components of the circulation can be obtained unequivocally using Lagrangian analysis. Here, we focus on the throughflow component of the freshwater transport, which, in the Atlantic is dominated by the Bering Strait throughflow.

Although Bering Strait is less than 100-km wide at its narrowest point and only 60-m deep at its deepest, its throughflow plays a direct role in the stability of the AMOC (De Boer & Nof, 2004; Hu et al., 2007; Hu & Meehl, 2005). Bering Strait also influences the freshwater distribution in the northern North Atlantic Ocean and the AMOC, by contributing to the freshwater budget, sea-ice formation and retreat, and freshwater export rate in the Arctic Ocean (Aagaard & Carmack, 1989; Aagaard et al., 2006; Hu et al., 2015; Proshutinsky & Johnson, 1997; Prinsenberg & Hamilton, 2005; Serreze et al., 2006, 2016; Timmermans & Marshall, 2020; R. A. Woodgate et al., 2010; R. Woodgate, 2013). Dramatic climate events observed during the past glacial periods, related to abrupt changes in the MOC, such as Dansgaard-Oeschger Events and Heinrich events (Dansgaard et al., 1993; Heinrich, 1988), might have occurred because Bering Strait was closed by the low sea level at that time (Hu et al., 2012). All indications are that the freshwater flux associated with Bering Strait throughflow is an important component in the global freshwater budget and influences the AMOC and the global MOC (Hu et al., 2015).

The net southward volume-flow through the Atlantic associated with Bering Strait throughflow and its northward counterpart in the Indo-Pacific poses a problem in the many estimates of the individual basin contributions to heat and freshwater transports (Ganachaud & Wunsch, 2000; Sloyan & Rintoul, 2001; Talley, 2008; Tsimplis et al., 1998; Wijffels et al., 2001): with a net flow through each basin, these transports depend on the arbitrary reference values for temperature and salinity (e.g., Talley, 2008), and so their contributions need to be accounted for and removed. In the Atlantic, the transport associated with Bering Strait throughflow is the largest component of the net volume throughflow, and this is the focus of our analysis.

One goal of our work is to attribute the contribution of Bering Strait throughflow to transports of volume, heat and freshwater in the Atlantic and Indo-Pacific basins, defined to be the respective sectors between 30° S and 65° N. The ocean north of 65° N is considered as the Arctic basin. In order to achieve this goal it is necessary to follow temperature and salinity on the paths of the Bering Strait throughflow throughout the global domain north of 30° S. This methodology differs fundamentally from the Eulerian approach, which identifies the different components of the flow by selected averages (i.e., averages over longitude, in depth or density coordinates) and the departures from these averages (Cessi, 2019; Piecuch et al., 2017).

One approach to study the paths of tracer transports of selected branches of the circulation is to use water-mass analysis, that is, tracer-based distributions, and tracer-based inverse box models (Arhan et al., 2003; Gebbie & Huybers, 2012; Johnson, 2008; Sloyan & Rintoul, 2001; Talley, 2008; Tsimplis et al., 1998; Well et al., 2003). A complementary approach is to use velocity-based Lagrangian analysis (Berglund et al., 2022; Blanke & Raynaud, 1997; Bower et al., 2019; Döös, 1995; Lozier et al., 2022; Rousselet et al., 2021, 2023): this is the method used in the following.

Our strategy is to release virtual parcels from Bering Strait, tracking their trajectories determined by three-dimensional velocity fields from ECCO (Estimating the Circulation and Climate of the Ocean, Forget et al., 2015). Conservation of mass requires that Bering Strait throughflow into the Arctic Ocean exits into the Atlantic Ocean, in addition to the small net freshwater input into the Arctic Ocean in the form of river runoffs and net precipitation (Aagaard & Carmack, 1989). Both backward tracking and forward tracking experiments are carried out and analyzed in a quasi-global domain: backward-tracking quantifies the pathways of Lagrangian parcels starting from the South Indo-Pacific Ocean; forward-tracking quantifies the fate of Lagrangian parcels from Bering Strait to the South Atlantic Ocean. With this information, together with the temperature and salinity fields along the parcels trajectories, the volume, heat and freshwater transports associated with Bering Strait throughflow can be estimated. Additionally, probability distributions of transit-times, thermohaline properties, and diapycnal transformation along the Lagrangian trajectories are diagnosed. The first moment of the distributions is the ensemble-average. Ensemble-averages complement Eulerian space or time averages.

This paper is organized as follows. Numerical experimental design, analysis, and data sets involved are discussed in Section 2. Transit-time distributions are discussed in Section 3. Paths and thermohaline properties of parcels are discussed in Section 4, and a discussion of heat and freshwater transport associated with Bering Strait throughflow is in Section 5. Conclusions are in Section 6.

2. Method and Data

Virtual-parcel releases are carried out with the offline version of the Massachusetts Institute of Technology General Circulation Model (MITgcm, using the OFFLINE and FLT packages, Marshall et al., 1997; Forget et al., 2015). Lagrangian parcels are advected by the monthly velocity field of ECCO, version 4 release 2, from year 1992 to 2011 (ECCO v4r2, Forget et al., 2015), on the native $1° \times 1°$-resolution grid in ECCO. The monthly velocity fields over the total 20 years are looped cyclically. Parcels are advected by the sum of Eulerian plus bolus velocity associated with the parametrization of isopycnal eddy-fluxes of tracers.

ECCO optimizes the following fields in order to minimize the model-data misfit: initial conditions (January 1992), surface boundary conditions, three-dimensional isopycnal and diapycnal diffusivity coefficients (Forget et al., 2015; Gent & McWilliams, 1990; Redi, 1982). The data sets used for this optimization include in-situ and remote observations (Forget et al., 2015, Tables 5 and 6). The model as configured in ECCO solves the hydrostatic, Boussinesq equations with exact budgets of volume, momentum, temperature, salinity and sea-ice (Marshall et al., 1997). ECCO version 4 uses the LLC90 (Longitude-Latitude-Cap 90) grid north of 57°N, to avoid numerical singularities at the North Pole. There have been collective efforts to show that the output of ECCO agrees with the climatology and variability of observations within uncertainties (e.g., Forget et al., 2015; L. Jackson et al., 2019).

The volume, heat and freshwater fluxes in ECCO across different gateways of the Arctic Ocean are compared in Table 1 to those in observations, in a higher resolution state estimate (Nguyen et al., 2021), and in a 4.5 km-resolution simulation (Wang et al., 2018). In ECCO, the residual of the outflow-minus-inflow through the Arctic gateways is −0.10 Sv, compensated by surface precipitation and runoff. Despite ECCO's horizontal resolution of 1°, the channels in Canadian Archipelago are open and the transport through Davis Strait is −1.5 Sv (southward), in agreement with observations (within uncertainties). As discussed in Section 4, Davis Strait is the main Arctic-Atlantic gateway for Bering Strait throughflow. The comparison in Table 1 shows agreements, within uncertainty, for all transports except for heat and freshwater transports at Davis Strait, which are underestimated by ECCO (Tesdal & Haine, 2020). We note that ECCO estimate encompasses all seasons for 20 years, while observations are scattered throughout the years and are primarily taken in summer. Most importantly, ECCO has closed budgets of volume, heat and salt, making it an appropriate tool to study the Bering Strait throughflow contribution to volume, heat and freshwater transports in the context of the global overturning circulation.

Parcels are released at a longitude-depth section located at 64.87°N in the North Pacific sector, slightly to the south of Bering Strait narrowest point, to avoid collisions with land soon after release. The release is effected once a month for the 20 years of ECCO v4r2 duration, to resolve the seasonal cycle and interannual variability. For all releases, parcels are randomly seeded in each south grid-face of the section, with the number of parcels proportional to the instantaneous meridional transport across each grid-face, following the "flux-weighting" method discussed by Döös (1995), Blanke and Raynaud (1997), and detailed in Appendix A.

Over the 240 months of ECCO data, a total of 293,417 parcels are released. The ensemble-averaged Lagrangian transport over this period is 1.04 Sv, comparable to the time-average observed value of approximately 1.0 Sv (e.g., R. A. Woodgate, 2018). The net transport across the initial section consists of 1.13 Sv northward transport and 0.09 Sv southward transport. Most of this southward transport is immediately recirculated northward, biasing the northward transport by a small overestimate. The ensemble-averaged distribution of released parcels in the longitude-depth plane is shown in Figure 1a. The histogram of initial transports of these parcels is shown in Figure 1b. The strength of initial transport for each parcel is almost constant, consistent with the "flux-weighting" method. At release, parcels carry generally cold and fresh North Pacific Waters (mode temperature and salinity: -1.96°C and 32.35 PSU) that are typical of Bering Strait throughflow (e.g., R. A. Woodgate, 2018).

Parcel trajectories are integrated with a 5-hr time-step. Parcels are tracked for a maximum of 1,000 years (backward in time), or for a maximum of 500 years (forward in time). The long integration times are reached by looping several times over the available velocity data (20 years for ECCO). The looping technique introduces errors, due to nonphysical jumps in some fields (the position is continuous, but the velocities and tracers are discontinuous at the end of each cycle). Because individual trajectories are chaotic and sensitive to initial conditions, only ensemble averages of Lagrangian quantities are meaningful. Looping errors have been quantified by Thomas et al. (2015): additional jumps are artificially introduced, but these jumps do not alter the ensemble

Table 1
Eulerian Volume (Sv), Heat (TW) and Freshwater (Liquid Only, mSv) Transports Through Arctic Gateways in ECCO V4r2; Arctic Subpolar Gyre sTate Estimate (ASTE); Observations; and 4.5 km-Resolution Numerical Model

Gateway	Transport of	ECCO	ASTE[a]	Observations	High-resolution model[d]
	Volume	1.04	1.1 ± 0.4	1.03 ± 0.05[b]	0.95
Bering Strait	Heat	6.32	5.6 ± 6.5	11.6 ± 0.61[b]	–
	Freshwater	76	52 ± 18	81 ± 4[b]	68
	Volume	−1.50	−1.7 ± 0.4	−1.7 ± 0.2[c]	−1.69
Davis Strait	Heat	8.99	20 ± 4	20 ± 9[e]	–
	Freshwater	−55	−88 ± 17	−98 ± 11[c]	−90
Fram Strait +	Volume	0.43	0.5 ± 1.4	1.2 ± 2.7[c]	0.68
Barents Sea Opening	Heat	117.06	101 ± 27	109 ± 6[f,g]	–
	Freshwater	−65	−49 ± 17	−90 ± 25[c]	−81

Note. In this table, the reference temperature for heat transport is 0°C, and reference salinity for freshwater transport is 34.8 PSU. [a]Nguyen et al. (2021). [b]R. A. Woodgate (2018). [c]Haine et al. (2015). [d]Wang et al. (2018). [e]Curry et al. (2011). [f]Schauer and Beszczynska-Möller (2009). [g]Rossby et al. (2018).

means. Thomas et al. (2015) concludes that errors in individual trajectories are averaged out as long as the statistics of the fields are stationary, and if a sufficiently high number of parcels are seeded. This is because, in the case of velocities with stationary statistics, a parcel restarted at the point **x** at the end of the velocity time-series can be relabeled and added to the ensemble of parcels passing at **x** at other times (Davis, 1991).

A trajectory is stopped when it crosses for the first time 30°S, in the Indo-Pacific sector for backward in time, and in the Atlantic sector for forward in time. A sample trajectory is shown in Figure 2, starting from 30°S in Indo-Pacific Ocean and ending at 30°S in the Atlantic Ocean (trajectory in South Pacific Ocean is shown "forward" in time). The large transformations seen in Figure 2 around years 175, 242 and 250 do not coincide with end-of-the-loop times, but are due to diapycnal transformation resolved during an ECCO cycle. The diapycnal transformation around year 175 is associated with the shoaling of the trajectory in the subpolar gyre of the North Pacific. The diapycnal transformations in years 242 and 250 are associated with deep water formation near Greenland. The statistics of these transformations are discussed in Sections 4.1 and 4.2.

Time-series of longitude, latitude, depth, temperature, salinity and pressure are stored on parcel trajectories at monthly intervals. In the analysis and discussion that follow, we exclude parcels that: (a) have not reached the section at 30°S by the end of the integrations; (b) have collided with bathymetry; (c) have flown back through

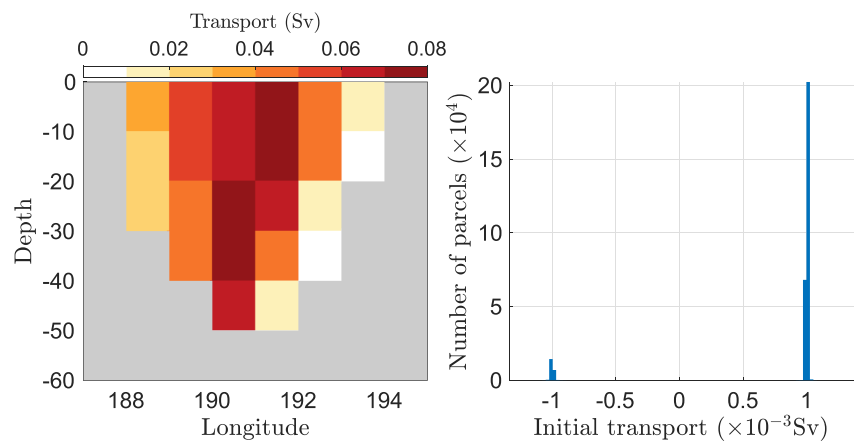

Figure 1. Transport distributions at the initial release location of Lagrangian parcels. (Left) Number of parcels, weighted by transport, binned in the longitude-depth plane according to ECCO's south grid-faces, ensemble-averaged over 240 months. The gray shading denotes the land mask. (Right) Histogram of initial transport of the Lagrangian parcels, for all 240 months of release.

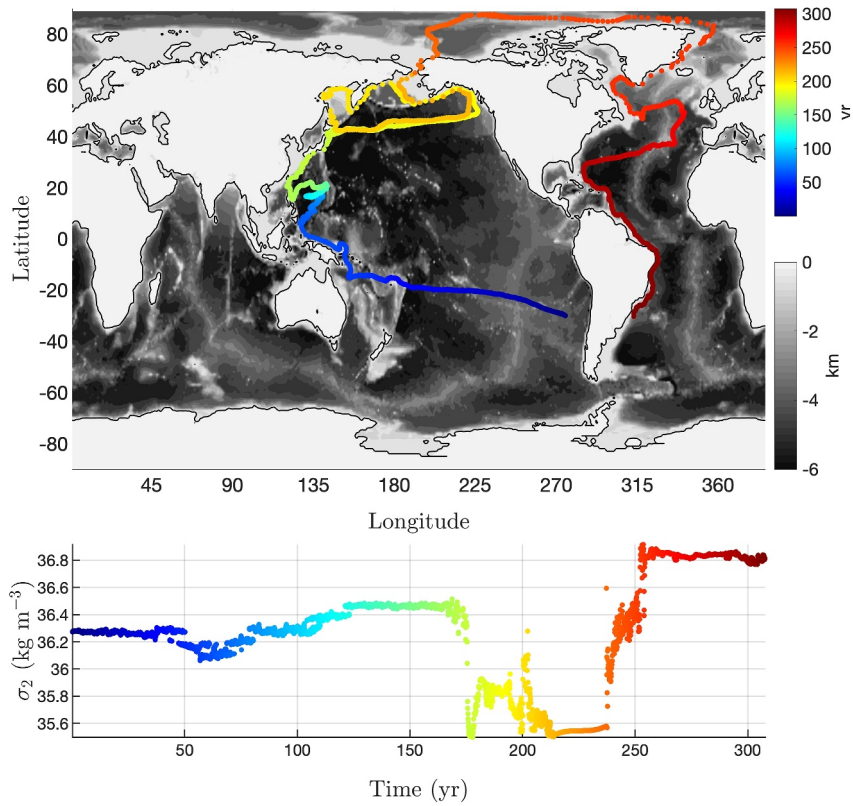

Figure 2. (Upper panel) Sample trajectory starting at 30°S in the Pacific sector and ending at 30°S in the Atlantic sector. (Lower panel) time-series of σ_2 along the trajectory. The progression is shown forward in time. Colors: time in years; gray shading: bathymetry in kilometers; black contours: surface coastline.

Bering Strait *before* crossing the 30°S sections first (i.e., flowing northward in backward trajectories, and southward in forward trajectories). Backward-in-time first passages correspond to last passages forward in time. Ideally, the no-flow and no-slip boundary conditions should prevent any encounter of parcel trajectories with solid walls, but parcels occasionally collide with bathymetry due to the discretization of the Lagrangian trajectory equations. Since only 2% of released parcels intersect bathymetry, excluding the parcels with these erroneous encounters does not affect the statistics.

3. Transit-Time Distributions

At the end of forward-tracking trajectories (500 years maximum), 0.91 Sv has crossed 30°S in the Atlantic, while at the end of backward-tracking trajectories 0.86 Sv has crossed 30°S in the Indo-Pacific. The transit-times distributions between Bering Strait and 30°S are shown in Figure 3: the median transit time, T^{50}, is 160 years for forward tracking trajectories and is 175 years for backward tracking. The 10-percentile transit time, T^{10}, is obviously shorter: 80 years for forward tracking and 60 years for backward tracking. The transit-time distribution between 65°N and 30°S in the Atlantic (forward trajectories originating at Bering Strait) is shown in Figure S1 in Supporting Information S1. The median transit time, T^{50}, is 135 years and the 10-percentile transit-time, T^{10}, is 55 years (cf. Figure S1 in Supporting Information S1). Because the Bering Strait throughflow is transported in the lower branch of the AMOC, these transit-times are also representative of the AMOC lower branch in ECCO.

The decay of the transit-time distributions are assessed by fitting power-laws to the tails of the distributions. For forward-tracking trajectories, the optimal decay between 300 and 500 years is $t^{-1.05}$. For backward-tracking trajectories the optimal decay between 300 and 500 years is $t^{-1.70}$, and between 501 and 1,000 years it is $t^{-0.99}$. In both cases, the tail of the distributions decay approximately as $1/t$, because of trapping around the edges of the wind-driven gyres. Neither backward nor forward trajectories have entered an exponential-decay regime in the transit-time distribution by the end of our computations. Given the slow decay between 500 and 1,000 years of the

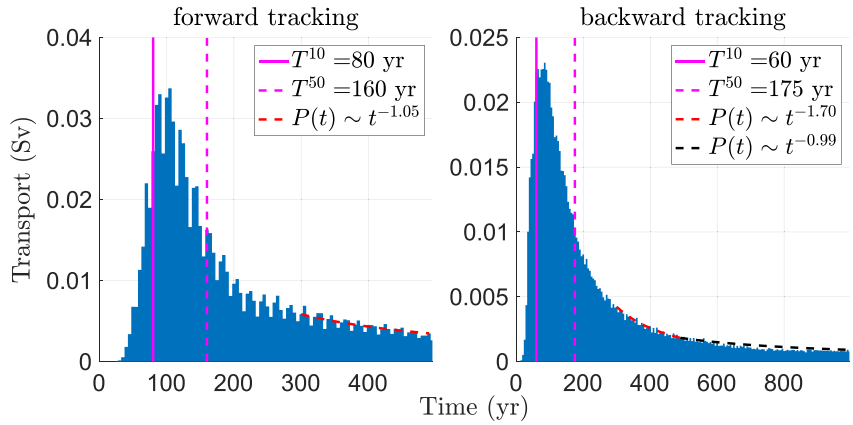

Figure 3. Transit-time distributions for first passage from release section at Bering Strait to 30°S, in the Atlantic sector (forward tracking, left panel) and for last passage in the Indo-Pacific sector (backward tracking, right panel), in 10-year bins. Magenta dashed line: median transit-time $\left(T^{50}\right)$. Magenta solid line: 10-percentile transit time $\left(T^{10}\right)$. Red dashed curve: power-law best-fit to the tail of the distribution from year 300–500; black dashed curve: power-law best-fit to the tail of the distribution from year 501–1,000.

backward trajectories, the forward trajectories are stopped at 500 years. In both cases, parcels that do not reach 30°S by the end of the computations spend many circuits within wind-driven gyres, or along the slow moving flow near the eastern boundary (cf. Figure S2 in Supporting Information S1): these are the flows that dominate the tails of the transit-times distributions (Bower et al., 2019). Because the Indo-Pacific is wider than the Atlantic, but the gyral velocities are comparable in the two basins, parcels are trapped for longer times in the Indo-Pacific gyres.

We use the information on the decay rate of the distribution to estimate a lower bound of how long it would take to recover 99% of the initial transport in both backward and forward trajectories. It would take over 4,955 years of additional integration to recover 99% of the backward trajectories, and over 680 additional years to recover 99% of the forward trajectories. In Section 4, statistics are calculated using the distributions shown in Figure 3, because it is only for these trajectories that we have full information on position and property distributions. In Section 5 we rescale the vertically and zonally integrated property transports to account for the total volume of Bering Strait throughflow, because this diagnostic requires a more limited amount of information than the maps shown in the following. Because the property transport diagnostics are compared to their Eulerian counterparts, the full Bering Strait transport needs to be accounted for.

4. Paths and Thermohaline Properties Along Trajectories

4.1. Indo-Pacific Ocean and Atlantic Ocean

In this section, we show horizontal maps of quantities on parcel trajectories, ensemble-averaged in $1° \times 1°$ longitude-latitude bins, including: (a) temperature (Θ); (b) salinity (S); (c) potential density (σ_2), (d) depth and (e) watermass transformations measured by diapycnal transport across a selected σ_2-surface. Ensemble-averaged zonal and meridional transports are also calculated in $1° \times 1°$ longitude-latitude bins (Appendix A). Streamfunction can then be calculated by spatially integrating the zonal or meridional transports following Blanke and Raynaud (1997). In the streamfunction calculations, an arbitrary constant can be set on any continuously connected boundary: our choice is to set this constant to zero along the continuously connected boundary comprising the western boundary of the Atlantic Ocean, the southern side of the Arctic Ocean and the eastern boundary of the Pacific Ocean. The results of backward- and forward-trajectories are combined in the maps shown in the following sections.

Bering Strait throughflow enters the Pacific basin in a broad layer near the eastern boundary at 30°S, at depths above 1 km (Figure 4, left panel, and black contours in Pacific Ocean in Figure 5). Parcels flow northwestward following the wind-driven gyres in the South Pacific, before recirculating in the tight zonally elongated gyres near the equator (Figure 5, black contours). Parcels eventually flow northward in the western boundary current

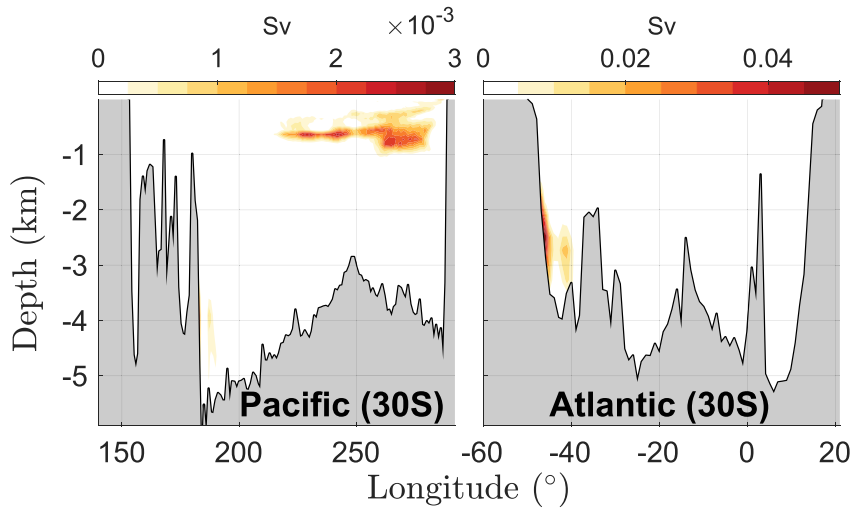

Figure 4. Longitude-depth sections at 30°S of ensemble-averaged parcel transports binned in 1° longitude and the 50 unevenly-spaced levels of the ECCO vertical gris in the Indo-Pacific sector (left panel), and in the Atlantic sector (right panel).

between 20°N and 40°N, and eastward along the western boundary current extension between 40°N and 52°N. Northward of 52°N, parcels flow northward near the eastern boundary, with most of the transport approaching Bering Strait along the coast of Alaska, consistent with the results of R. A. Woodgate (2018).

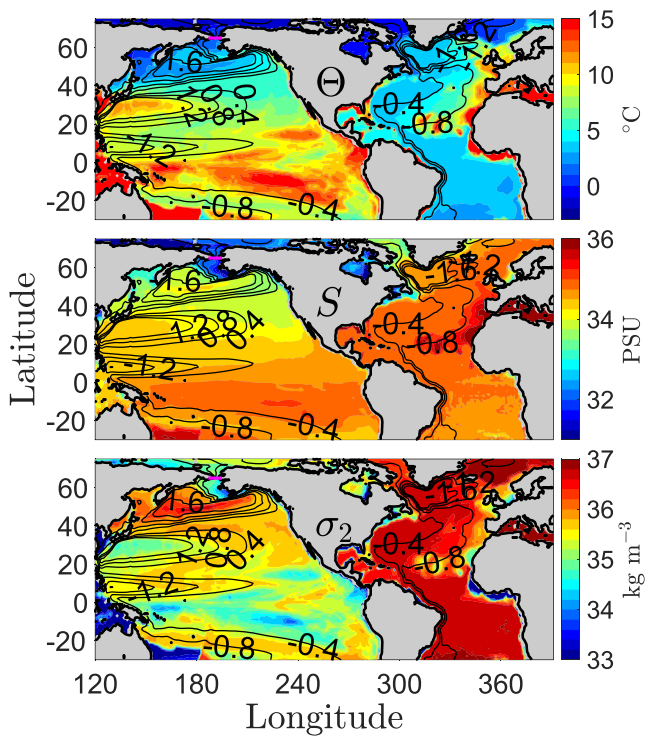

Figure 5. Horizontal maps of ensemble-averaged variables (colors) following parcel trajectories between the last passage (in the Indo-Pacific) and the first passage through 30°S section, and streamfunction (black contours), in the backward- and forward-trajectories. (Top) temperature; (middle) salinity; (bottom) σ_2. Ensemble-averages in the Indo-Pacific are calculated from backward trajectories, and those in the Atlantic Ocean are calculated from forward trajectories. The Indian sector is not shown because less than 0.5% parcels end up there.

Along their way northward, some parcels circulate in the subtropical and subpolar gyres in the North Pacific Ocean (closed contours in Figure 5). Note that since we only consider parcels that reach the 30°S section from Bering Strait before the end of the experiments, each parcel trajectory is open. These closed contours appear because streamfunctions are integrated in depth. Therefore, the vertical spiraling and ultimate escape of all parcels from the gyres can be lost in the map of streamfunctions.

In the Pacific, the parcels become colder and fresher as they proceed northward (Figure 5, color shading in top and middle panels). The net result is a progressive densification along trajectories (Figure 5, bottom panel), except very close to Bering Strait. As trajectories exit the Alaskan coast toward the Arctic, they shoal and get fresh: it is in this region, very close to Bering Strait itself, that the throughflow properties are determined (Figure 5 middle panel, and Figure S3 in Supporting Information S1).

Parcels enter the northern North Atlantic from both the Labrador and Greenland Seas (Figure 5). Parcels then flow southward along the western boundary, recirculating in the subpolar gyre north of 45°N. In this gyre, parcels become slightly warmer, saltier, and denser. Between 45°N and 20°N the flow primarily occurs on the eastern side of North Atlantic. Southward of 20°N, parcels proceed southward as a component of Deep Western Boundary Current (DWBC), that is, in the lower branch of the AMOC (Bower et al., 2019; Talley, 2013). Parcels ultimately exit the South Atlantic at 30°S at depths between 2 and 4 km, dominantly along the western boundary (Figures 4, right panel, and S3 in Supporting Information S1).

A comparison with previous estimates of North Atlantic pathways from Arctic gateways is not straightforward because previous work has focused mostly on the overflow east of Greenland (Lozier et al., 2022), while two thirds of our Lagrangian parcels enter the North Atlantic from Davis Strait.

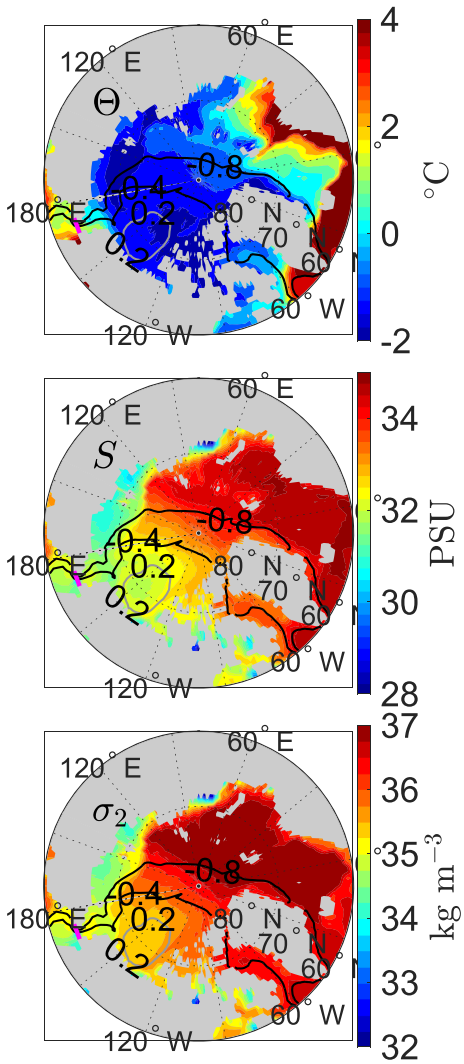

Figure 6. Polar-view maps of ensemble-averaged properties binned in $1° \times 1°$ of latitude-longitude, following the forward trajectories in the Arctic Ocean. The magenta line denotes the location of the initial release at Bering Strait. Black and gray contours: streamfunction. Black contours: positive streamlines with interval of 0.4 Sv; gray contour: one negative streamline of 0.2 Sv. Colors: (Top) Temperature; (middle) salinity; (bottom) σ_2.

Focusing on the lower part of the southward AMOC branch, isobaric RAFOS floats (not Lagrangian parcels) have been released at densities $\sigma_2 > 37.06$ (Lozier et al., 2022), and the majority of these floats flow southward west of the Middle Atlantic Ridge. In contrast, the average of our Lagrangian floats entering the North Atlantic have $\sigma_2 < 37.0$ (cf. bottom panel of Figure 5 and the blue hues in Figure 8). These more buoyant Lagrangian parcels are steered by the subtropical gyre more effectively, and thus flow southward preferentially east of the Middle Atlantic Ridge between 45°N and 20°N, than the whole of the lower branch of the AMOC considered by Lozier et al. (2022).

A comparison of ensemble-averaged thermohaline properties between the Pacific versus the Atlantic reveals that parcels are warmer and fresher, and thus lighter in the Pacific. Therefore, we anticipate a net northward transport of both heat and freshwater associated with Bering Strait throughflow, as quantified in Section 5.

4.2. Parcel Paths in the Arctic Ocean and Deep Water Formation

Davis Strait and the Greenland Sea are the final gateways for Arctic freshwater fluxes to enter the North Atlantic (Aksenov et al., 2016; Karami et al., 2021; Østerhus et al., 2019), with Bering Strait throughflow as the principal component of the freshwater transport. Lagrangian analysis shows that parcels that ultimately enter the Labrador Sea are colder and fresher compared to those entering through the Greenland Sea (Figure 6). This is because of the intrusion of warm and salty Atlantic Waters east of Greenland (Aagaard et al., 1985). Approximately one quarter of the parcels recirculate in the Beaufort gyre (Figure 6, gray contour), lenghtening the residence time in the Arctic.

The parcels entering the North Atlantic from Bering Strait are classified to come from either the Labrador Sea or the Greenland Sea. The histogram at 65°N as a function of longitude (in 1° bins) is shown in Figure 7, upper panel. There is a 0.58 Sv southward transport entering from the Labrador Sea and a 0.33 Sv sothward transport from the Greenland Sea, that is, 64% from the Labrador side and 36% East of Greenland. This partition of the Bering Strait throughflow, combined with the total Eulerian transport estimates shown in Table 1 (0.5 Sv northward flow east of Greenland and −1.7 Sv of southward flow west of Greenland), indicates that there is a cyclonic loop around Greenland carrying about (0.5 + 0.33)Sv = 0.83 Sv. This current carries warm and saline waters from the North Atlantic around Greenland, opposing the cold and fresh water southward transport effected by the Bering Strait throughflow.

A measure of deep water formation is the ensemble-averaged transport across an isopycnal: here we chose the diapycnal transport across $\sigma_2 = 36.75$ kg m^{-3} (positive upwards), as representative of deep water formation (Figure 7 bottom panel). This measure of transformation shows densification preferentially occurring in the southern coast of Greenland.

A summary of $\Theta - S$ properties for parcels at different sections in Figure 8 offers an additional view of the transformation along the trajectories. Relative to Bering Strait (red hues and red circle), parcels are saltier and denser at 65°N in the Labrador sea (purple hues and triangle), but warmer, saltier, and denser in the Greenland Sea (pink hues and star). The smaller density difference between Bering Strait and Labrador Sea is consistent with more transport exported though this path (Figure 7, top panel). The large difference between Bering Strait and the Greenland Sea is consistent with mixing with northward flowing waters coming from the North Atlantic.

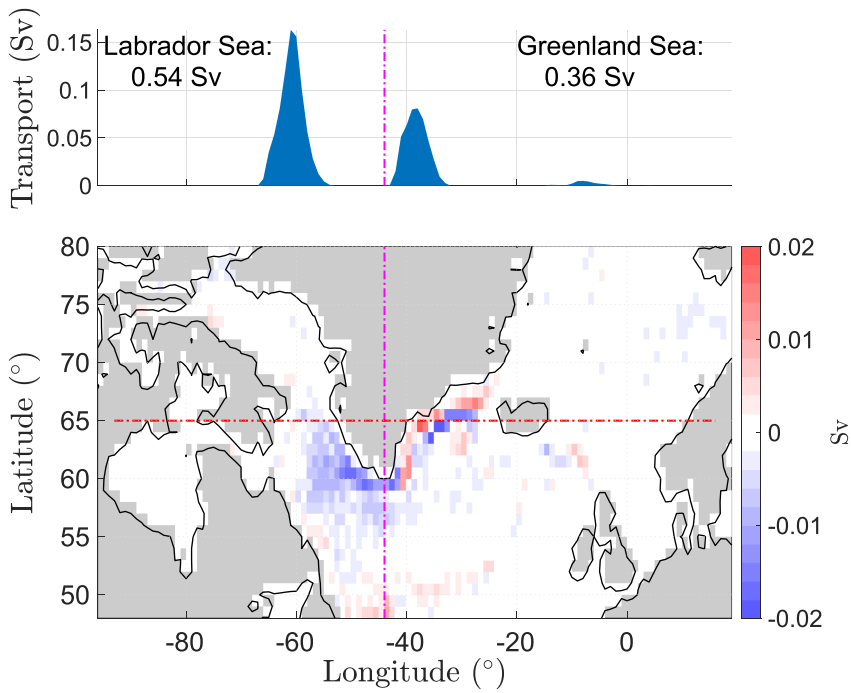

Figure 7. (Top) Transport-weighted histogram of first time parcel-crossing 65°N (southward) into North Atlantic in 1° longitudinal bins. (Bottom): Colors: ensemble-averaged diapycnal transport as parcels cross the isopycnal $\sigma_2 = 36.75$ kg m^{-3} (positive upwards) in $1° \times 1°$ bins. Red line: the 65°N section in northern North Atlantic; Magenta line: longitude of −50°, the boundary between "Labrador Sea" and "Greenland Sea." Gray areas are either land or bins with less than 100 parcel occurrences.

From the Labrador and Greenland Sea sections, parcels gradually densify to 30°S in the South Atlantic (blue colors and diamond). From these two northern sources, the density difference between Labrador Sea and 30°S is larger, consistent with the large signal of deep water transformation near the Labrador Sea, south of Davis Strait.

At 30°S in the Atlantic sector (Figure 8, blue hues), the mode temperature and salinity are 3.14°C and 34.90 PSU. These values are in the range of North Atlantic Deep Water (Talley, 2011). In the South Pacific Ocean (Figure 8, green hues), the mode temperature and salinity are 5.94°C, 34.25 PSU, typical for Antarctic Intermediate Water (Talley, 2011). Consistent with Figure 5, Bering Strait throughflow comes from a relatively shallow branch of the South Pacific circulation, and ends as a component of the lower branch of AMOC.

5. The Bering Strait Throughflow Component of Heat and Freshwater Transports

Following Appendix A, we quantify heat and freshwater transports associated with Lagrangian parcels using

$$Q_{hBST}(y) = c_p \rho_0 \sum_{n=1}^{N_p} \sum_{m=1}^{C_n} \Theta_{n,\,m} T_n \mathrm{sign}(v_{n,m}), \tag{1}$$

$$Q_{fBST}(y) = \sum_{n=1}^{N_p} \sum_{m=1}^{C_n} \left(1 - \frac{S_{n,\,m}}{S_0}\right) T_n \mathrm{sign}(v_{n,\,m}), \tag{2}$$

where Q_{hBST} and Q_{fBST} denote heat and freshwater transports summed over all parcels in 1°-latitude bins. The sums are for any longitude, depth and time in the Indo-Pacific for backward trajectories, and in the Atlantic Ocean for forward trajectories. $c_p = 4 \times 10^3$ Joules/kg/C and $\rho_0 = 1029$ kg/m^3 denote the heat capacity and reference density of sea water, respectively. N_p is the total number of parcels that have reached the 30°S section at the end of each experiment, and C_n is the number of latitude crossings for the n-th parcel. $\Theta_{n,\,m}$ and $S_{n,\,m}$ are temperature and salinity on trajectories at the time of latitude-crossing, T_n is the parcel's initial transport (conserved along the trajectory) and $\mathrm{sign}(v_{n,\,m})$ represents the crossing direction: +1 for northward or −1 for southward. $S_0 = 34.9$ is

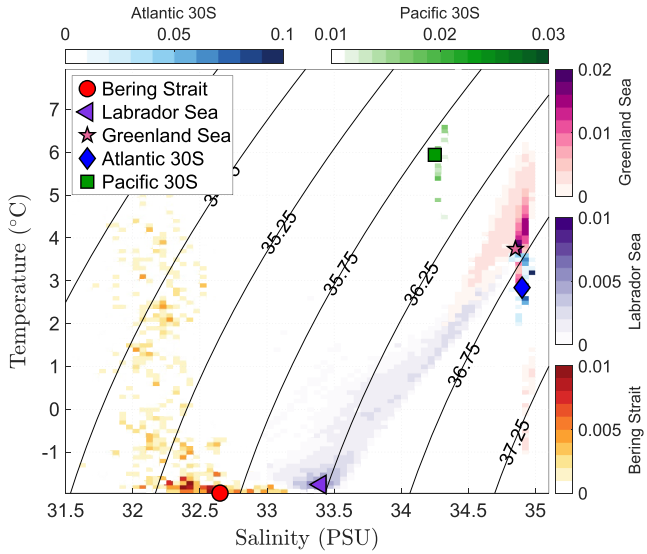

Figure 8. Two-dimensional histogram of parcel frequency (weighted by transport) in temperature-salinity space at various sections. Colors are in Sverdrup. Red hues: at Bering Strait; green hues: backward-tracking parcels crossing the 30°S in the Indo-Pacific; blue hues: forward-tracking parcels as they first cross the 30°S section in the Atlantic; purple hues: as forward-tracking parcels enter North Atlantic from Labrador Sea at 65°N); pink hues: as forward-tracking parcels first enter North Atlantic from Greenland Sea at 65°N. Black contours: σ_2. Colored markers: mode temperature and salinity. Bering Strait: $\Theta = -1.96$°C, $S = 32.35$PSU, $\sigma_2 = 35.50$ kg m^{-3}); Pacific 30S: $\Theta = 5.94$°C, $S = 34.25$PSU, $\sigma_2 = 35.97$ kg m^{-3}; Atlantic 30S: $\Theta = 3.14$°C, $S = 34.90$PSU, $\sigma_2 = 36.93$ kg m^{-3}; Labrador Sea:$\Theta = -1.76$°C, $S = 33.40$PSU, $\sigma_2 = 36.32$ kg m^{-3}; Greenland Sea: $\Theta = 3.84$°C, $S = 34.90$PSU, $\sigma_2 = 36.82$ kg m^{-3}.

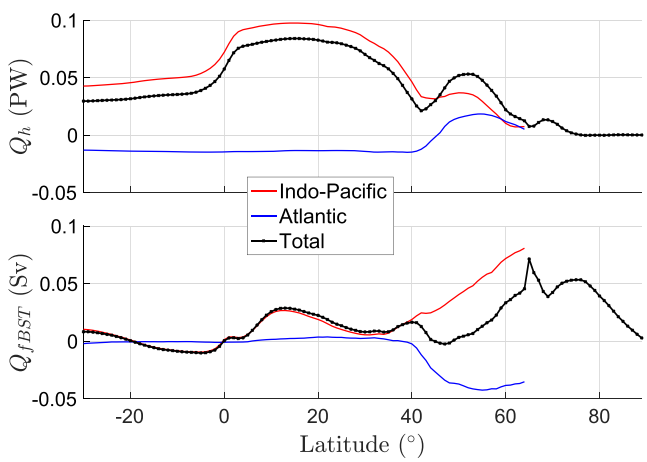

Figure 9. Heat (top panel) and freshwater Lagrangian transports (bottom panel) in the Pacific Ocean (red lines), Atlantic Ocean (blue lines) and total (Pacific plus Atlantic, black line), ensemble-averaged in 1° of latitude bins for all longitudes, depths and time.

the reference salinity, as used by Talley (2008). The simple formula to convert freshwater transports (FW) with different salinity references is simply

$$\mathrm{FW}_1 = \frac{S_2}{S_1}(\mathrm{FW}_2 - V) + V, \tag{3}$$

where V is the volume transport. We prefer to show freshwater transport, rather than salt transport, because the former is closer to salinity transport in models with a free surface and volume-flux exchanges at the surface, such as ECCO. Salt transport is associated with the small salt input by brine rejection during sea-ice formation and is less relevant to the transport of salinity (Schauer & Losch, 2019; Tréguier et al., 2014).

In order to have net property transports that are independent of the reference value, the northward and southward volume transports must be equal and opposite. However, our forward and backward trajectories do not recover the full Bering Strait throughflow in the time allowed for the integration, and the fraction recovered differs between the two directions. To address this problem we rescale the initial transports attributed to each parcel, so as to account for the total Bering Strait throughflow in both forward and backward trajectories. In other words, we consider the parcels that do not reach 30°S as "lost" and redistribute the initial transport among the remaining successful parcels. We are reassured that this procedure is unbiased because we repeated the heat and freshwater transport calculations, including all the parcels that reach 40°N, which carry 100% of the northward volume transport at Bering Strait (1.13 Sv). The heat and freshwater transport thus obtained, rescaled to the net volume transport at Bering Strait (1.04 Sv), are within 5% of the values obtained with the subset of parcels that reach 30°S, when appropriately rescaled to have the same volume transport.

The net heat transport associated with Bering Strait throughflow is northward everywhere (Figure 9, top panel, black curve). This is because northward-moving parcels in the Indo-Pacific are warmer than southward-moving parcels in the Atlantic at every latitude (Figure 5, top panel, and Figure 8, blue and green hues). The strength of the heat transport is a small fraction of the heat carried by the AMOC, which, in ECCO, peaks at 0.9PW at 20°N (Piecuch et al., 2017; Piecuch & Ponte, 2012). North of 45°N the recirculation in the Atlantic subpolar gyre transports warm waters northward, and cold waters southward, resulting in a northward heat transport that enhances the northward heat flux from the Pacific Ocean. The net northward heat transport by the Bering Strait throughflow is dominated by the Pacific sector contribution (red curve in the top panel of Figure 9). The heat carried into the Arctic from the Pacific is relevant to Arctic sea-ice formation and retreat (e.g., Serreze et al., 2016; R. A. Woodgate et al., 2010).

The net freshwater transport due to Bering Strait throughflow is northward over most latitudes (Figure 9, bottom panel, black curve) because the northward volume transport in the Pacific sector carries fresher water than the southward volume transport in the Atlantic (cf. Figure 5, middle panel, and 8, blue and green hues). In each basin-sector, the freshwater transport is substantial only in the subpolar region and Arctic. It is northward in the Indo-Pacific, but southward in the subpolar Atlantic region. This is because there is southward transport of freshwater on the western side of the subpolar gyre, but northward transport of saltier water on the eastern side (cf. the middle panel of Figure 4).

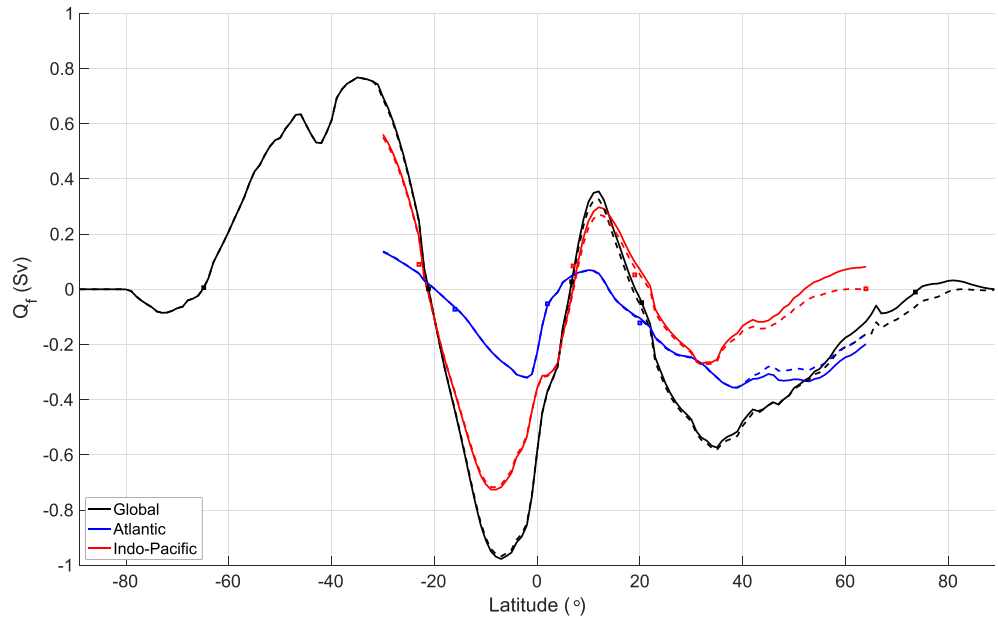

Figure 10. Vertically and zonally integrated and time-averaged advective Eulerian freshwater transports from ECCO, Q_f, for the global ocean (black solid lines). Global Q_f minus Q_{fBST} (blacked dashed line). The black square markers denote the latitudes where the volume transport, Q_v, vanishes and Q_f is independent of the salinity reference value (set at $S_0 = 34.9$). Differences $Q_f - Q_{fBST}$ for the Indo-Pacific sector (red dashed line), and Atlantic sector (dashed blue lines). The red and blue square markers denote the latitude where the volume transports equal the Bering Strait throughflow, that is, $Q_v = \pm 1.04Sv$ (negative sign for blue squares and positive sign for red squares). At these latitudes the Eulerian and Lagrangian estimates carry the same volume flux.

The contribution by Bering Strait throughflow to the Eulerian global and sector transports, associated with all processes, is complicated by net zonally and vertically integrated volume transports that balance surface freshwater fluxes, both in each basin sector and in the global integral. Because of these volume transports and the Bering Strait throughflow, Eulerian property fluxes depend on the arbitrary reference values for Θ and S. The Eulerian volume transports for ECCO, defined as

$$Q_v(y) \equiv \int dx \int dz\, v, \tag{4}$$

are shown in Figure S4 in Supporting Information S1 (the integrals are taken over all depths, and over all longitudes either in the global domain or in basin-sector subdomains). There are a few latitudes where the global Q_v vanishes: these are the latitudes where the global heat and freshwater transports are independent of the reference values for Θ and S. In the Atlantic, Q_v varies about 30% around the Bering Strait throughflow, while in the Indo-Pacific the differences are larger, reducing the volume transport to 0.26 Sv near 10° S. This is due to the large catchment area for precipitation in the warm pool region, which reduces the northward volume transport associated with Bering Strait throughflow.

Figure 10 (black solid curve) shows the time-averaged Eulerian freshwater transport for ECCO, Q_f, defined as

$$Q_f(y) \equiv \int dx \int dz\, v\left(1 - \frac{S}{S_0}\right), \tag{5}$$

with $S_0 = 34.9$ PSU (Talley, 2008). The black squares indicate the latitudes where $Q_v = 0$. To understand the importance of the freshwater transport effected by the Bering Straight throughflow, we subtract the Lagrangian contribution Q_{fBST} shown in Figure 9 (bottom panel, black curve) from Q_f (solid black curve in Figure 10). The resulting freshwater transport (dashed black curve in Figure 10) differs from the total freshwater transport in the

subpolar and Arctic latitudes: in the Indo-Pacific north of 50°N, Q_{fBST} is of the same order as Q_f. In the Arctic, we attribute the residual southward freshwater transport to the cyclonic loop current around Greenland, which transports salty waters of North Atlantic origin east of Greenland and fresh waters of Arctic origin in the Labrador Sea: in Section 4.2, we estimated the loop current to transport about 0.8 Sv cyclonically.

The skeptical reader can focus only on the latitudes marked by black squares: at these points the Eulerian freshwater transport has zero net volume transport, is independent of the reference salinity, and can be meaningfully compared to the Lagrangian freshwater transport, Q_{fBST}, which has zero net volume transport at all latitudes.

The difference $Q_f - Q_{fBST}$ for the Indo-Pacific sector (red dashed lines) and for the Atlantic sector (blue dashed lines) are also shown in Figure 10. In each basin sector, the red and blue square markers denote the latitudes where the Eulerian volume transports equal the Bering Strait throughflow Lagrangian transport ($\pm$1.04 Sv, plus sign for the Indo-Pacific and minus sign for the Atlantic sectors). At these latitudes the volume transports of each basin sector coincide for the Lagrangian and Eulerian estimates, so it is meaningful to compare the total Eulerian freshwater transport with the Lagrangian freshwater transport by the Bering Strait throughflow alone. The important point is that subtracting Q_{fBST} from Q_f reduces the freshwater transport in the subpolar North Pacific to near zero, demonstrating the importance of the Bering Strait throughflow in the freshwater budget in this region as concluded by Talley (2008). The contribution of the Bering Strait throughflow in the subpolar region of the North Atlantic is more muted. In this region, the contribution of the Bering Strait throughflow amplifies the salt-advection feedback, by making the freshwater transport more negative.

6. Conclusion

The transport of mass (volume), temperature and freshwater associated with the Bering Strait throughflow, as quantified by Lagrangian analysis, is part of the global mid-depth overturning cell. The northward branch of this component is in the upper layer of Pacific, while the southward branch is in the lower branch of AMOC.

Although velocities decay with depth, the northward transit time from 30° S to 65° N in the Pacific sector are longer (median is 175 years) than their southward counterpart in the Atlantic (median is 135 years). The Pacific transit times are lengthened by long recirculations around the upper ocean gyres, while the Atlantic transit times are sped up by efficient transport in the DWBC, primarily south of 20° N.

The heat and freshwater transports of the Bering Strait component are a miniature version of their AMOC counterpart: the net transport of heat and freshwater is northward. The contribution of Bering Strait throughflow to the Pacific and Atlantic heat and freshwater transports is small, except in the subpolar region: here the Bering Strait throughflow adds a non-negligible contribution to the northward freshwater transport in the Pacific sector. In the Atlantic sector the Bering Strait contribution adds about 20% to the southward freshwater transport in the subpolar gyre, that is, in the same direction as the freshwater transport by the AMOC.

The paths of the Bering Strait throughflow into the Atlantic, combined with the volume budget of Nguyen et al. (2021), highlight a cyclonic recirculation of North Atlantic water around Greenland, which preconditions the transformation of Bering Strait throughflow water in the Labrador Sea. Consistently, our analysis identifies the exit region of the Labrador Sea as the principal site of transformation into NADW of the Bering Strait contribution.

Because of the net volume transport across basins, freshwater and heat transports depend on the reference levels of salinity and temperature, respectively. The largest component of the net volume transport is associated with Bering Strait throughflow, and our work has quantified this contribution. The relative smallness of this contribution, except in the subpolar regions, vindicates the Eulerian procedure commonly used to eliminate this component to evaluate the AMOC and gyral contributions (Cimatoribus et al., 2012; Piecuch et al., 2017). We speculate that the freshwater and heat transports due to the volume transport of precipitation minus evaporation, which is smaller than the Bering Strait throughflow, can also be eliminated by removing the barotropic component of the volume transport, without incurring in substantial errors.

Appendix A: Lagrangian Analysis Approach

A1. Equivalence of Parcels Concentration and Conserved Tracer

Lagrangian analysis, using discrete parcels and their concentration, is equivalent to the following procedure for a conserved tracer. Consider a section at fixed latitude y_o. At the initial time t_o "paint" a grid-face of area $\Delta x_o\ \Delta z_o$, centered at the point x_o, y_o, z_o with "dye" for a short time Δt. The amount of dye entering the domain of interest is proportional to $\Delta y_o = v(x_o, y_o, z_o, t_o)\Delta t$, that is, there is more dye where the velocity $v(x_o, y_o, z_o, t_o)$ is larger. Without diffusion and for incompressible flow, the initial painted volume is conserved following the flow, although it will be stretched and folded, that is,

$$\frac{D\ v(x_o, y_o, z_o, t_o)\Delta x_o\ \Delta z_o \Delta t}{Dt} = 0. \tag{A1}$$

Choosing a constant Δt for all positions along the initial section, the conservation statement (Equation A1) is equivalent to conservation of the initial transport at each dye release location, that is,

$$\frac{D\ T_o}{Dt} = 0, \quad \text{with } T_o \equiv v(x_o, y_o, z_o, t_o)\Delta x_o\ \Delta z_o. \tag{A2}$$

Using parcels instead of dye, an individual fraction of transport, T_n, conserved along the trajectory, can be attributed to each of the parcels seeded at the initial grid-face according to

$$T_n = \frac{T_o}{N_o}. \tag{A3}$$

Because of the conservation statement (Equation A2), the number N_o of parcels seeded in the initial grid-volume, $T_o \Delta t$, should be proportional to T_o, so as to make T_n approximately constant among all parcels seeded. This "flux-weighting" constraint is necessary to ensure that the initial parcel concentration (i.e., the released "dye") is consistent with the notion that there is more dye (or more parcels) where $v(x_o, y_o, z_o, t_o)$ is larger, and thus satisfying (Equations A1 and A2).

The procedure outlined above for a single grid-face is repeated for each grid-face of the section, and, for time-dependent velocities, for each time necessary to describe the velocity time-series. Because the resulting trajectories are sensitive to the initial condition, and thus chaotic, each grid-face is seeded at different initial positions, even if the velocity is constant within the grid-face. Because of the sensitivity to initial conditions, it is unnecessary to sample the time-dependent initial velocity on time-scales shorter than the initial velocity decorrelation times.

Velocities are interpolated in time and space to accurately calculate the trajectory, and the spatial interpolation scheme must preserve the incompressibility condition of the velocity field, in order to satisfy (Equations A1 and A2).

The ensemble-averaged quantities are defined on a binned mesh grid along all trajectories as

$$\langle C \rangle = \frac{\sum_n \sum_m T_n C_{nm}}{\sum_n T_n}, \tag{A4}$$

where the sum in n is over the parcels arriving in each bin and the sum in m is the number of occurrence in each bin per parcel. If second-moments (or higher-order) statistics are needed, the interior velocity advecting the parcels must be sampled at short-enough times to capture velocity correlations. The ensemble-integrated horizontal transport of properties, $\langle (u, v)C \rangle$ can be calculated as

$$\langle (u, v)C \rangle = \sum_n \sum_m T_n C_{nm} \text{sign}(u_{nm}, v_{nm}), \tag{A5}$$

where the sum over n is taken over all parcels crossing a horizontal grid box. The sum over m is taken over all crossings, weighted by the sign of the velocity for each crossing (positive for northward or eastward). The transport, T_n, is determined at the seeding section according to (Equation A3), and conserved along the trajectory: it is part of parcel's label. The property, C_{nm}, is recorded along the trajectory and varies along the trajectory, except when considering volume transport, where $C_{nm} = 1$.

Maps of ensemble-averaged property transformations can be obtained through the relation

$$\frac{D\,C}{Dt} = \mathcal{D}_C \tag{A6}$$

where $\mathcal{D}_C$ are the sources and sinks of C. The left hand side of (Equation A6) can be evaluated by recording C at discrete time intervals along each trajectory and taking the ensemble over occurrences in desired spatial bins. If the discrete time intervals along each trajectory are uniform, then it is useful to record the difference between two consecutive times, ΔC, rather than the rate (Equation A6).

A2. Advantages of Lagrangian Parcel Analysis Over Passive Tracer Analysis

Lagrangian analysis bypasses the numerical difficulties encountered when solving advection of a tracer without diffusion. It is difficult to numerically solve

$$\partial_t C + \nabla \cdot \mathbf{v}C = 0, \tag{A7}$$

but it is simple to solve

$$\dot{\mathbf{x}} = \mathbf{v}(\mathbf{x}, \mathbf{t}). \tag{A8}$$

The advantage of solving (Equation A8) without diffusion is that transport of mass can be quantified (volume in the Boussinesq approximation). Transformation of tracers subject to diffusion (and other non conservative processes) can be diagnosed by recording the values of tracers along the parcel trajectories and using (Equation A6).

Finally, (Equation A8) is computationally more efficient than solving (Equation A7) for localized injections. It is not necessary to solve equations at grid points that have no parcels (or no tracer): the computational power is localized to the parcels' locations. Additionally, (Equation A8) is typically solved using high order time-stepping schemes (e.g., fourth order Runga-Kutta), allowing longer time steps than those necessary to satisfy the Courant–Friedrichs–Lewy condition in (Equation A7).

Data Availability Statement

The MITgcm model used for this work is available for download from https://github.com/rousseletL/MITgcm_flt_Rousselet2020. ECCO version 4 release 2 data are available from ftp://mit.ecco-group.org/ecco_for_las/version_4/release4/. All data, MITgcm modifications, numerical outputs, and analysis scripts used in this work, are archived in the "Open Science Framework," which is a public, community-supported repository, at https://osf.io/4b26u/. These codes are publicly available, with no restrictions.

Acknowledgments
Paola Cessi and Xiaoting Yang are supported by NASA Grant 80NSSC20K0796 and NSF Grant OCE-2421170. We would like to acknowledge high-performance computing from Cheyenne and Derecho provided by NCAR's Computational and Information System Laboratory. The suggestions and highsights by two anonymous reviewers are gratefully acknowledged.

References

Aagaard, K., & Carmack, E. C. (1989). The role of sea ice and other fresh water in the Arctic circulation. *Journal of Geophysical Research*, *94*(C10), 14485–14498. https://doi.org/10.1029/jc094ic10p14485

Aagaard, K., Swift, J., & Carmack, E. (1985). Thermohaline circulation in the Arctic mediterranean seas. *Journal of Geophysical Research: Oceans*, *90*(C3), 4833–4846. https://doi.org/10.1029/jc090ic03p04833

Aagaard, K., Weingartner, T. J., Danielson, S. L., Woodgate, R. A., Johnson, G. C., & Whitledge, T. E. (2006). Some controls on flow and salinity in Bering Strait. *Geophysical Research Letters*, *33*(19). https://doi.org/10.1029/2006gl026612

Aksenov, Y., Karcher, M., Proshutinsky, A., Gerdes, R., De Cuevas, B., Golubeva, E., et al. (2016). Arctic pathways of Pacific water: Arctic Ocean model intercomparison experiments. *Journal of Geophysical Research: Oceans*, *121*(1), 27–59. https://doi.org/10.1002/2015jc011299

Arhan, M., Mercier, H., & Park, Y.-H. (2003). On the deep water circulation of the eastern South Atlantic Ocean. *Deep Sea Research Part I: Oceanographic Research Papers*, *50*(7), 889–916. https://doi.org/10.1016/s0967-0637(03)00072-4

Berglund, S., Döös, K., Groeskamp, S., & McDougall, T. J. (2022). The downward spiralling nature of the north Atlantic subtropical gyre. *Nature Communications*, *13*(1), 2000. https://doi.org/10.1038/s41467-022-29607-8

Blanke, B., & Raynaud, S. (1997). Kinematics of the pacific equatorial undercurrent: An Eulerian and Lagrangian approach from GCM results. *Journal of Physical Oceanography*, *27*(6), 1038–1053. https://doi.org/10.1175/1520-0485(1997)027<1038:kotpeu>2.0.co;2

Bower, A., Lozier, S., Biastoch, A., Drouin, K., Foukal, N., Furey, H., et al. (2019). Lagrangian views of the pathways of the Atlantic meridional overturning circulation. *Journal of Geophysical Research*, *124*(8), 5313–5335. https://doi.org/10.1029/2019jc015014

Cessi, P. (2019). The global overturning circulation. *Annual Review of Marine Science*, *11*(1), 249–270. https://doi.org/10.1146/annurev-marine-010318-095241

Cimatoribus, A. A., Drijfhout, S. S., den Toom, M., & Dijkstra, H. A. (2012). Sensitivity of the Atlantic meridional overturning circulation to South Atlantic freshwater anomalies. *Climate Dynamics*, *39*(9–10), 2291–2306. https://doi.org/10.1007/s00382-012-1292-5

Curry, B., Lee, C., & Petrie, B. (2011). Volume, freshwater, and heat fluxes through Davis Strait, 2004–05. *Journal of Physical Oceanography*, *41*(3), 429–436. https://doi.org/10.1175/2010jpo4536.1

Dansgaard, W., Johnsen, S. J., Clausen, H. B., Dahl-Jensen, D., Gundestrup, N., Hammer, C. U., et al. (1993). Evidence for general instability of past climate from a 250-kyr ice-core record. *Nature*, *364*(6434), 218–220. https://doi.org/10.1038/364218a0

Davis, R. E. (1991). Observing the general circulation with floats. *Deep Sea Research Part A. Oceanographic Research*, *38*, S531–S571. https://doi.org/10.1016/s0198-0149(12)80023-9

De Boer, A. M., & Nof, D. (2004). The Bering Strait's grip on the northern hemisphere climate. *Deep Sea Research Part I: Oceanographic Research Papers*, *51*(10), 1347–1366. https://doi.org/10.1016/j.dsr.2004.05.003

Döös, K. (1995). Interocean exchange of water masses. *Journal of Geophysical Research*, *100*(C7), 13499–13514. https://doi.org/10.1029/95jc00337

Drijfhout, S. S., Weber, S. L., & van der Swaluw, E. (2011). The stability of the MOC as diagnosed from model projections for pre-industrial, present and future climates. *Climate Dynamics*, *37*(7–8), 1575–1586. https://doi.org/10.1007/s00382-010-0930-z

Ferreira, D., Cessi, P., Coxall, H., de Boer, A., Dijkstra, H., Drijfout, S., et al. (2018). Atlantic-Pacific asymmetry in deep water formation. *Annual Review of Earth and Planetary Sciences*, *46*(1), 327–352. https://doi.org/10.1146/annurev-earth-082517-010045

Forget, G., Campin, J.-M., Heimbach, P., Hill, C., Ponte, R., & Wunsch, C. (2015). Ecco version 4: An integrated framework for non-linear inverse modeling and global ocean state estimation. *Geoscientific Model Development*, *8*(10), 3071–3104. https://doi.org/10.5194/gmd-8-3071-2015

Ganachaud, A., & Wunsch, C. (2000). Improved estimates of global ocean circulation, heat transport and mixing from hydrographic data. *Nature*, *408*(6811), 453–457. https://doi.org/10.1038/35044048

Gebbie, G., & Huybers, P. (2012). The mean age of ocean waters inferred from radiocarbon observations: Sensitivity to surface sources and accounting for mixing histories. *Journal of Physical Oceanography*, *42*(2), 291–305. https://doi.org/10.1175/jpo-d-11-043.1

Gent, P. R., & McWilliams, J. C. (1990). Isopycnal mixing in ocean circulation models. *Journal of Physical Oceanography*, *20*(1), 150–155. https://doi.org/10.1175/1520-0485(1990)020<0150:imiocm>2.0.co;2

Haine, T. W., Curry, B., Gerdes, R., Hansen, E., Karcher, M., Lee, C., et al. (2015). Arctic freshwater export: Status, mechanisms, and prospects. *Global and Planetary Change*, *125*, 13–35. https://doi.org/10.1016/j.gloplacha.2014.11.013

Heinrich, H. (1988). Origin and consequences of cyclic ice rafting in the Northeast Atlantic Ocean during the past 130,000 years. *Quaternary Research*, *29*(2), 142–152. https://doi.org/10.1016/0033-5894(88)90057-9

Hu, A., & Meehl, G. A. (2005). Bering Strait throughflow and the thermohaline circulation. *Geophysical Research Letters*, *32*(24). https://doi.org/10.1029/2005gl024424

Hu, A., Meehl, G. A., & Han, W. (2007). Role of the Bering Strait in the thermohaline circulation and abrupt climate change. *Geophysical Research Letters*, *34*(5). https://doi.org/10.1029/2006gl028906

Hu, A., Meehl, G. A., Han, W., Abe-Ouchi, A., Morrill, C., Okazaki, Y., & Chikamoto, M. O. (2012). The Pacific-Atlantic seesaw and the Bering Strait. *Geophysical Research Letters*, *39*(3). https://doi.org/10.1029/2011gl050567

Hu, A., Meehl, G. A., Han, W., Otto-Bliestner, B., Abe-Ouchi, A., & Rosenbloom, N. (2015). Effects of the Bering Strait closure on AMOC and global climate under different background climates. *Progress in Oceanography*, *132*, 174–196. https://doi.org/10.1016/j.pocean.2014.02.004

Jackson, L., Dubois, C., Forget, G., Haines, K., Harrison, M., Iovino, D., et al. (2019). The mean state and variability of the North Atlantic circulation: A perspective from ocean reanalyses. *Journal of Geophysical Research: Oceans*, *124*(12), 9141–9170. https://doi.org/10.1029/2019jc015210

Jackson, L. C., & Wood, R. A. (2018). Timescales of AMOC decline in response to fresh water forcing. *Climate Dynamics*, *51*(4), 1333–1350. https://doi.org/10.1007/s00382-017-3957-6

Johnson, G. C. (2008). Quantifying antarctic bottom water and north Atlantic deep water volumes. *Journal of Geophysical Research: Oceans*, *113*(C5). https://doi.org/10.1029/2007jc004477

Karami, M. P., Myers, P. G., de Vernal, A., Tremblay, L. B., & Hu, X. (2021). The role of arctic gateways on sea ice and circulation in the Arctic and North Atlantic oceans: A sensitivity study with an ocean-sea-ice model. *Climate Dynamics*, *57*(7), 2129–2151. https://doi.org/10.1007/s00382-021-05798-6

Lozier, M. S., Bower, A. S., Furey, H. H., Drouin, K. L., Xu, X., & Zou, S. (2022). Overflow water pathways in the North Atlantic. *Progress in Oceanography*, *208*, 102874.

Marshall, J., Adcroft, A., Hill, C., Perelman, L., & Heisey, C. (1997). Hydrostatic, quasi-hydrostatic and nonhydrostatic ocean modeling. *Journal of Geophysical Research*, *102*(C3), 5733–5752. https://doi.org/10.1029/96jc02776

Mecking, J., Drijfhout, S. S., Jackson, L. C., & Graham, T. (2016). Stable AMOC off state in an eddy-permitting coupled climate model. *Climate Dynamics*, *47*(7–8), 2455–2470. https://doi.org/10.1007/s00382-016-2975-0

Nguyen, A. T., Pillar, H., Ocaña, V., Bigdeli, A., Smith, T. A., & Heimbach, P. (2021). The arctic subpolar gyre state estimate: Description and assessment of a data-constrained, dynamically consistent ocean-sea ice estimate for 2002–2017. *Journal of Advances in Modeling Earth Systems*, *13*(5), e2020MS002398. https://doi.org/10.1029/2020ms002398

Østerhus, S., Woodgate, R., Valdimarsson, H., Turrell, B., De Steur, L., Quadfasel, D., et al. (2019). Arctic mediterranean exchanges: A consistent volume budget and trends in transports from two decades of observations. *Ocean Science*, *15*(2), 379–399. https://doi.org/10.5194/os-15-379-2019

Piecuch, C. G., & Ponte, R. M. (2012). Importance of circulation changes to Atlantic heat storage rates on seasonal and interannual time scales. *Journal of Climate*, *25*(1), 350–362. https://doi.org/10.1175/jcli-d-11-00123.1

Piecuch, C. G., Ponte, R. M., Little, C. M., Buckley, M. W., & Fukumori, I. (2017). Mechanisms underlying recent decadal changes in subpolar North Atlantic Ocean heat content. *Journal of Geophysical Research: Oceans*, *122*(9), 7181–7197. https://doi.org/10.1002/2017jc012845

Prinsenberg, S., & Hamilton, J. (2005). Monitoring the volume, freshwater and heat fluxes passing through Lancaster sound in the Canadian Arctic archipelago. *Atmosphere-Ocean*, *43*(1), 1–22. https://doi.org/10.3137/ao.430101

Proshutinsky, A. Y., & Johnson, M. A. (1997). The circulation regimes of the wind-driven Arctic Ocean. *Journal of Geophysical Research*, *102*(C6), 12493–12514. https://doi.org/10.1029/97jc00738

Rahmstorf, S. (1996). On the freshwater forcing and transport of the Atlantic thermohaline circulation. *Climate Dynamics*, *12*(12), 799–811. https://doi.org/10.1007/s003820050144

Redi, M. H. (1982). Oceanic isopycnal mixing by coordinate rotation. *Journal of Physical Oceanography*, *12*(10), 1154–1158. https://doi.org/10.1175/1520-0485(1982)012<1154:oimbcr>2.0.co;2

Rossby, T., Flagg, C., Chafik, L., Harden, B., & Søiland, H. (2018). A direct estimate of volume, heat, and freshwater exchange across the Greenland-Iceland-Faroe-Scotland ridge. *Journal of Geophysical Research*, *123*(10), 7139–7153. https://doi.org/10.1029/2018jc014250

Rousselet, L., Cessi, P., & Forget, G. (2021). Coupling of the mid-depth and abyssal components of the global overturning circulation according to a state estimate. *Science Advances*, *7*(21), eabf5478. https://doi.org/10.1126/sciadv.abf5478

Rousselet, L., Cessi, P., & Mazloff, M. R. (2023). What controls the partition between the cold and warm routes in the meridional overturning circulation? *Journal of Physical Oceanography*, *53*(1), 215–233. https://doi.org/10.1175/jpo-d-21-0308.1

Schauer, U., & Beszczynska-Möller, A. (2009). Problems with estimation and interpretation of oceanic heat transport-conceptual remarks for the case of Fram Strait in the Arctic Ocean. *Ocean Science*, *5*(4), 487–494. https://doi.org/10.5194/os-5-487-2009

Schauer, U., & Losch, M. (2019). "Freshwater" in the ocean is not a useful parameter in climate research. *Journal of Physical Oceanography*, *49*(9), 2309–2321. https://doi.org/10.1175/jpo-d-19-0102.1

Serreze, M. C., Barrett, A. P., Slater, A. G., Woodgate, R. A., Aagaard, K., Lammers, R. B., et al. (2006). The large-scale freshwater cycle of the Arctic. *Journal of Geophysical Research: Oceans*, *111*(C11). https://doi.org/10.1029/2005jc003424

Serreze, M. C., Crawford, A. D., Stroeve, J. C., Barrett, A. P., & Woodgate, R. A. (2016). Variability, trends, and predictability of seasonal sea ice retreat and advance in the Chukchi sea. *Journal of Geophysical Research: Oceans*, *121*(10), 7308–7325. https://doi.org/10.1002/2016jc011977

Sloyan, B. M., & Rintoul, S. R. (2001). The Southern Ocean limb of the global deep overturning circulation. *Journal of Physical Oceanography*, *31*(1), 143–173. https://doi.org/10.1175/1520-0485(2001)031<0143:tsolot>2.0.co;2

Stommel, H. (1961). Thermohaline convection with two stable regimes of flow. *Tellus*, *13*(2), 224–230. https://doi.org/10.3402/tellusb.v13i2.12985

Talley, L. D. (2008). Freshwater transport estimates and the global overturning circulation: Shallow, deep and throughflow components. *Progress in Oceanography*, *78*(4), 257–303. https://doi.org/10.1016/j.pocean.2008.05.001

Talley, L. D. (2011). *Descriptive physical oceanography: An introduction*. Academic Press.

Talley, L. D. (2013). Closure of the global overturning circulation through the Indian, Pacific, and Southern Oceans: Schematics and transports. *Oceanography*, *26*(1), 80–97. https://doi.org/10.5670/oceanog.2013.07

Tesdal, J.-E., & Haine, T. W. N. (2020). Dominant terms in the freshwater and heat budgets of the subpolar North Atlantic Ocean and Nordic Seas from 1992 to 2015. *Journal of Geophysical Research*, *125*(10), e2020JC016435. https://doi.org/10.1029/2020jc016435

Thomas, M. D., Tréguier, A.-M., Blanke, B., Deshayes, J., & Voldoire, A. (2015). A Lagrangian method to isolate the impacts of mixed layer subduction on the meridional overturning circulation in a numerical model. *Journal of Climate*, *28*(19), 7503–7517. https://doi.org/10.1175/jcli-d-14-00631.1

Timmermans, M.-L., & Marshall, J. (2020). Understanding Arctic Ocean circulation: A review of ocean dynamics in a changing climate. *Journal of Geophysical Research: Oceans*, *125*(4), e2018JC014378. https://doi.org/10.1029/2018jc014378

Tréguier, A.-M., Deshayes, J., Le Sommer, J., Lique, C., Madec, G., Penduff, T., et al. (2014). Meridional transport of salt in the global ocean from an eddy-resolving model. *Ocean Science*, *10*(2), 243–255. https://doi.org/10.5194/os-10-243-2014

Tsimplis, M., Bacon, S., & Bryden, H. (1998). The circulation of the subtropical South Pacific derived from hydrographic data. *Journal of Geophysical Research*, *103*(C10), 21443–21468. https://doi.org/10.1029/98jc01881

Wang, Q., Wekerle, C., Danilov, S., Wang, X., & Jung, T. (2018). A 4.5 km resolution Arctic Ocean simulation with the global multi-resolution model FESOM 1.4. *Geoscientific Model Development*, *11*(4), 1229–1255. https://doi.org/10.5194/gmd-11-1229-2018

Well, R., Roether, W., & Stevens, D. P. (2003). An additional deep-water mass in Drake passage as revealed by ^{3}He data. *Deep Sea Research Part I: Oceanographic Research Papers*, *50*(9), 1079–1098. https://doi.org/10.1016/s0967-0637(03)00050-5

Wijffels, S. E., Toole, J. M., & Davis, R. (2001). Revisiting the South Pacific subtropical circulation: A synthesis of world ocean circulation experiment observations along 32S. *Journal of Geophysical Research*, *106*(C9), 19481–19513. https://doi.org/10.1029/1999jc000118

Woodgate, R. (2013). Arctic Ocean circulation: Going around at the top of the world. *Nature Education Knowledge*, *4*(8), 8. Retrieved from https://www.nature.com/scitable/knowledge/library/arctic-oceancirculation-going-around-at-the-102811553

Woodgate, R. A. (2018). Increases in the pacific inflow to the arctic from 1990 to 2015, and insights into seasonal trends and driving mechanisms from year-round Bering Strait mooring data. *Progress in Oceanography*, *160*, 124–154. https://doi.org/10.1016/j.pocean.2017.12.007

Woodgate, R. A., Weingartner, T., & Lindsay, R. (2010). The 2007 Bering Strait oceanic heat flux and anomalous arctic sea-ice retreat. *Geophysical Research Letters*, *37*(1). https://doi.org/10.1029/2009gl041621